Interaction of the Cyprus/Tethys slab with the mantle transition zone beneath Anatolia

George Taylor[1†], David A. Thompson[2$], David Cornwell[3], Sebastian Rost[1*]

[1] School of Earth and Environment, University of Leeds, Woodhouse Lane, Leeds, LS2 9JT, United Kingdom
[2] School of Earth and Ocean Sciences, Cardiff University, Park Place, Cardiff, CF10 3AT
[3] School of Geosciences, University of Aberdeen, King's College, Aberdeen, AB24 3UE
[$] formerly at School of Geosciences, University of Aberdeen, King's College, Aberdeen, AB24 3UE and School of Earth and Environment, University of Leeds, Woodhouse Lane, Leeds, LS2 9JT, United Kingdom
† Now at Institute of Seismology, School of Geosciences and Geography, University of Helsinki, Helsinki, Finland.

[*]Corresponding author: Sebastian Rost (S. Rost), s.rost@leeds.ac.uk, School of Earth and Environment, University of Leeds, Woodhouse Lane, Leeds, LS2 9JT, United Kingdom

Accepted:
Received:
In Original Form:

Abbreviated title: Mantle Transition Zone beneath Anatolia

Last Update: 06/12/18 9:22 AM

Summary

The interaction of subducted oceanic lithosphere with the discontinuities of the mantle transition zone (MTZ) provides insight into the composition and temperature of the subducted slab as well as potential melting of the slab or the surrounding mantle and loss of volatiles from the slab. Detailed mapping of the structure of the MTZ will help to better understand how slabs transport material and volatiles into the mantle and how phase transitions affect the slab dynamics. Here we use a dense network of seismic stations in northern Anatolia to image the structure of the MTZ discontinuities in detail using P-wave receiver functions. With a station spacing of about 7 km and a surface footprint of ~35 km by ~70 km, analysing receiver functions calculated from teleseismic earthquakes that occurred during an ~18 month deployment produced clear images of where the mantle transition zone interacts with the Tethys/Cyprus slabs that either lie flat on the 660-km discontinuity or pass into the lower mantle. We observe an undulating 660-km discontinuity depressed by up to 30 km and a slightly depressed (1 – 2 km) 410-km discontinuity, apparently undisturbed by the slab. The

MTZ is thickened to ~270 km as result of the cool slab in the MTZ influencing the 660-km discontinuity and includes an arrival at ~520-km depth likely from the top of a flat lying slab or a discontinuity related to a solid-solid phase transition in the olivine component of the mantle. We find evidence for low-velocity zones both above and below the 410-km discontinuity and above the 660-km discontinuity. The low velocity zones around the 410-km discontinuity might be the result of hydration of the MTZ from the slab and upward convection of MTZ material into the upper mantle. The origin of the low velocity zone around the 660-km discontinuity is less clear and could be related to sedimentation of subducted mid-ocean ridge basalts. The small footprint of the seismic array provides accurate information on the structure of the MTZ in an area influenced by subduction and shows small-scale changes in MTZ structure that might be lost in studies covering larger areas with sparser sampling.

Keywords: Mantle Processes, Phase Transitions, Composition & Structure of the Mantle, Dynamics of Lithosphere & Mantle, Subduction Zone Processes

Introduction

Subducted slabs are a major pathway for oceanic lithosphere, continental sediments, and volatiles to be transported into the lower mantle. Constraining this process and the interaction of the slab with the mantle at different depths is essential for our understanding of the flux and storage of elements such as carbon and water into the lower mantle and has an impact on life and the long-term habitability of Earth (Dasgupta and Hirschmann, 2010; Schmandt et al., 2014). The upper mantle beneath the eastern Mediterranean has long been influenced by interactions with subducted material due to the closure of the Tethys ocean and the on-going subduction at the Hellenic and Cyprus trenches (Cavazza et al., 2004; Faccenna et al., 2006; Jolivet et al., 2013; Robertson and Dixon, 1984; Stampfli, 2000). It is therefore an ideal location to study the interaction of subducted material with the upper mantle.

The mantle transition zone (MTZ) is bounded by two global seismic discontinuities located at depths of approximately 410 km and 660 km. These sharp increases in seismic velocity are typically attributed to solid-solid phase transitions in the olivine component of the mantle. The 410-km discontinuity (herewith ‘the 410’) marks the transition from α-olivine to wadsleyite, whilst the 660 km discontinuity (herewith ‘the

660') is due to a transition from ringwoodite to bridgmanite and magnesiowüstite (Frost, 2008). The depths of the 410 and 660 transitions are dependent on pressure and temperature (e.g. *Helffrich*, 2000), allowing MTZ thickness to be used to infer the thermal state of the mantle (Flanagan and Shearer, 1998; Schmerr and Garnero, 2006; Shearer and Masters, 1992). The 410 transition occurs at lower pressures (and hence at shallower depths) in the presence of lower temperatures, while the opposite Clapeyron slope of the 660 means it will occur deeper in regions of lower temperature (e.g. *Helffrich*, 2000). Increased temperatures will conversely result in a deeper 410, and a shallower 660, resulting in a thinned MTZ. Theoretical and experimental studies on the petrology of upper mantle material have also shown that the composition and water content of the mantle strongly influence the structure and depth of these discontinuities (Bolfan-Casanova et al., 2006).

An additional discontinuity at a depth of about 520 km (the 520) has also been observed at several locations (Shearer, 1990) and might be related to the wadsleyite to ringwoodite phase transition (Sinogeikin, 2003) or the formation of $CaSiO_3$ bridgmanite from garnet (Saikia et al., 2008). The 520 has been found to occur over a diffuse depth range and therefore might not be sharp enough to observe seismically and observations remain controversial (Bock, 1994). The 520 might be observable in subduction zones (Gilbert et al., 2001) where the wadsleyite-ringwoodite phase transition may occur over a small pressure interval due to variations in olivine content (Gu et al., 1998), hydrated mantle or slab material (Inoue et al., 1998).

Mineral-physical studies have shown that water content influences the properties of the olivine-wadsleyite phase transition (Ohtani, 2005; Smyth and Frost, 2002). Water is preferentially incorporated into wadsleyite rather than olivine, so the transition zone has a larger water storage capability than the upper or lower mantle. This could lead to dehydration melting in material moving upwards through the 410, or sinking through the 660 (Bercovici and Karato, 2003; Revenaugh and Sipkin, 1994; Schmandt et al., 2014). It is possible that the related partial melting could be observed as zones of low seismic velocity bounding the transition zone discontinuities (Revenaugh and Sipkin, 1994).

The eastern Mediterranean has a long and complex tectonic history currently characterized by differential plate motions between Arabia/Eurasia and by active subduction at the Hellenic and Cyprus trenches (Pichon and Angelier, 1979; Pichon et al., 1981). It has been proposed that the material being subducted at these trenches is

some of the oldest oceanic lithosphere on the planet and might be a remnant of the closure of the Neo- and Paleo-Tethys oceans (Granot, 2016; Hafkenscheid et al., 2006).

Tomographic images of the upper mantle in the region show the location of the subducted material from the active trenches to the top of the lower mantle (Berk Biryol et al., 2011; Bijwaard et al., 1998; Fichtner et al., 2013a, 2013b; Goes et al., 1999; Paul et al., 2014; Piromallo and Morelli, 2003; Salaün et al., 2012; Zhu et al., 2015), with evidence for a long lasting tear in the slab at the Isparta angle influencing the dynamics of the region (Berk Biryol et al., 2011; Bijwaard et al., 1998; Jolivet et al., 2013, 2009). Although the tomographic images show that the flow of the eastern Mediterranean slabs into the lower mantle could be impeded by the 660 beneath Anatolia (Berk Biryol et al., 2011), the Tethys slab has been detected in the lower mantle beneath India (van der Meer et al., 2009; Van der Voo et al., 1999). It therefore remains unclear exactly how the slabs interact with MTZ discontinuities beneath Anatolia and the location where it penetrates into the lower mantle.

This study utilises P-wave receiver functions (e.g. *Langston*, 1979; *Ammon*, 1991) from a dense network of seismometers deployed in north-western Turkey to image the MTZ discontinuities beneath Anatolia (DANA, 2012). Our results show that the MTZ is thickened to ~270 km and contains a strong 520 km discontinuity, with evidence for multiple low velocity layers around the discontinuities. This provides conclusive evidence for the presence of the slab and indicates a complex interplay of processes as the slab interacts with the MTZ beneath Anatolia.

Data and Analysis

A temporary network (Fig. 1a) of 73 medium- and broad-band seismometers was deployed between May 2012 to October 2013 across the North Anatolian Fault zone in the rupture zone of the 1999 Izmit earthquake (DANA, 2012). The stations were deployed on a semi-regular rectangular grid of 6 lines East-West and 11 rows North-South. The nominal station spacing of the regular grid is 7 km. In addition to the main grid, a further 7 stations were deployed in a half circle towards the east, with a larger station spacing.

We use instrument-response deconvolved P-waveforms from 160 high-quality teleseismic events (Fig. 1b) to compute P-wave receiver functions (PRF), isolating P-to-S wave conversions from seismic discontinuities beneath the array. The waveform

data were initially filtered using a second-order Butterworth band-pass filter between 0.04 Hz and 3.0 Hz. We used an iterative time domain deconvolution method (Ligorría and Ammon, 1999) with a Gaussian pulse width of 0.625 to deconvolve the vertical component P waveform from both the radial and transverse components to isolate P-to-S wave conversions from the MTZ discontinuities. This approach leads to a dominant receiver function frequency of ~0.3 Hz, which is the ultimate limit on the spatial resolution of this study. Whilst the nature of our array (station spacing of ~7 km) provides us with dense sampling within the MTZ (Fig. 1b), our horizontal resolution is limited by the size of the Fresnel zone radii within the MTZ (approximately 60-80 km). Visual inspection led to 2346 high-quality receiver functions sampling an area of ~3° by 3° where slabs from the Mediterranean subduction zones (Hellenic and Cyprus slabs) have been imaged within the MTZ (*Berk Biryol et al*., 2011; Fig. 1b). This dataset was further trimmed to 1505 of the highest quality PRFs following an automated signal-to-noise ratio procedure (Cornwell et al., 2011; Hetényi et al., 2009). The final dataset of PRFs is dominated by ray paths that sample the MTZ to the north and east of the array (Fig. 1b). This ray geometry provides sampling in the region where the Hellenic and Cyprus slabs interact with the 660 discontinuity, while not sampling the transition of the slab through the 410 to the south of the region sampled by our dataset. Figures for the full dataset are shown in the supplemental material with images produced with the quality selected dataset shown in the main part of the manuscript.

PRFs were then migrated using three different approaches to firstly characterise the broad features and then examine their variation in space and depth. The first method is a 1D time migration (Stoffa et al., 1981) (Fig. 2) without corrections for crust and upper mantle velocity variations (Thompson et al., 2011) assuming the 1D Earth model ak135 (Kennett et al., 1995). We then perform a 2-D common conversion point (CCP) migration (Sheehan et al., 2000) in depth again using the ak135 velocity model (Fig. 3). This migration collapses all the data from our small conversion point footprint into a 2D N-S profile, with a minimum of 10 conversion points in an individual bin. Finally, we perform a 3D CCP migration (Fig. 4) through the EU60 velocity model of *Zhu et al*. [2015] by binning into 15 x 15 x 2 km voxels and then accounting for the Fresnel zone size by applying a Gaussian smoothing operator over

5 (i.e. 75 km) neighbouring bins in the horizontal directions and 3 (i.e. 6 km) in the vertical direction (e.g. Hetényi et al., 2009).

Results

The PRF results clearly show P-to-S conversions from the upper mantle discontinuities. Figure 2a shows stacked PRFs as a function of slowness. An Nth-root (N=4) slant stack for a reference slowness of 5.59 s/deg showing the observed seismic arrivals is also included in Fig. 2b. The P-to-S conversions from the 410 and 660 are clearly visible arriving at ~45 s and ~65 s, slightly later (~2-3 s) than predicted by ak135. This could be due to the low S-wave velocities in the upper mantle beneath Anatolia (Fichtner et al., 2013a; Salaün et al., 2012; Zhu et al., 2015), but our dataset cannot rule out the possibility that both the 410 and 660 are located slightly deeper than average in this location. Notably, the traveltime anomalies are consistent between the 410 and 660 arrival times, which suggests that the majority of this travel time residual can be accounted for through velocity variations in the upper mantle above the 410 along the S-leg of the P-to-S conversion. Another positive arrival is located at times between 50 and 60 s, between the 410 and 660. The arrival time of this arrival varies as a function of slowness, arriving earlier at low slowness, and later at slownesses of greater than 6.5 s/deg. This arrival is most likely a P-to-S conversion from a discontinuity at approximately 520 km depth, potentially related to the wadsleyite to ringwoodite transition. We also observe a lower amplitude positive arrival at 75–85 s, which corresponds to a lower mantle depth of ~800 km (Figs. 2 and 4). In addition to these positive arrivals, there are several negative arrivals present in the PRFs that suggest velocity decreases with depth (i.e. a low velocity layer). These negative arrivals are particularly prominent at ~40 s and ~50 s, bounding the 410 discontinuity. A further localised negative arrival can be seen above the 660 at ~65 s, most evident at a slowness of larger than +6.5 s/deg. The moveout characteristics of these arrivals indicate that they are not multiples from shallower discontinuities (Fig. 2b).

The results of the 2D and 3D CCP depth migrations are shown in Figs. 3 and 4, overlain onto the EU60 tomography model (Zhu et al., 2015). Vertical and horizontal resolution of these migrated receiver function images are estimated to be +/-5 km and 30 km, respectively, based on the first Fresnel Zone at the relevant frequency. The 410 shows little depth variation along the 2D radial PRF profile whereas the 660

shows minor undulations on the order of 10 km (Fig 3). The maximum thickness of the transition zone in this transect is ~270 km: thicker than the global average of 242 km (Gu and Dziewonski, 2002). This thickening is the result of topography and an overall deepening of the 660, which is largest close to the subducted slab indicated by high seismic velocities in the tomographic model. A conversion from a depth of ~520 km is visible in the centre of the profile (Fig. 3), close to the velocity gradient interpreted as the top of the slab in the EU60 tomography model (Zhu et al., 2015).

The 3D CCP depth migration using the EU60 tomography model (Fig. 4) generally displays similar structures to those observed in the 2D migrated profile (Fig. 3). Migration through the 3D tomography model appears to remove part of the traveltime anomaly visible in the 1D/2D migrations, giving further support to an upper mantle source of this traveltime anomaly. Some slight delay remains in the 3D migrated images, indicating that the tomography model may underpredict the magnitude of the upper-mantle velocity anomalies in the region. The 410 is enclosed by negative arrivals, which can also be seen above the 660. A positive arrival from ~520 km depth occurs at various locations, with a depth variation of +/-20 km. This arrival is strongest in the centre of the profiles coinciding with the top of the high velocity anomaly in the tomographic models. Negative arrivals around the 410 and 660 show clear lateral variations. The negative arrival above the 660 seems to be absent from the southern part of the profile, while the arrival from below the 410 is present almost everywhere. The arrival above the 410 appears more complex but is clearly visible in both the south and north of the profile.

Transverse PRFs were calculated using the deconvolution of the vertical from tangential components (see supplemental material) to examine evidence for radial seismic anisotropy or P-S conversions from dipping structures. Although some energy is present, the data distribution might prevent any conclusive interpretation of this energy and there seems to be little consistent structure throughout the volume in these transverse PRFs. We therefore conclude that there are no major and robust radially anisotropic signals present in the MTZ in this region.

Discussion

Our PRF results provide high-resolution images of the MTZ in the vicinity of a subducted slab. The tomographic models (shown in the background of Figures 2, 3 and 4) indicate that a slab (defined by the high velocity anomaly) is lying flat on the

660, although there is alternative evidence that it penetrates the lower mantle (Bijwaard et al., 1998; van der Meer et al., 2018; Zhu et al., 2015). Our densely sampled receiver function images allow new detailed insight into the physical processes occurring during the interaction of the slab with the MTZ (Fig. 5).

In general, the main features of the dataset are consistent between all migration approaches (Figs. 2,3 and 4), though some lateral variations in the MTZ structure are apparent in the 3D dataset. The amplitude of the 410 conversion is quite variable in the 3D migration, and is not clearly visible in the far west and east of the image (Fig. 4). In addition, the low velocity zone below the 410, that is prevalent throughout the 1D and 2D migrations, is notable only in the northern parts of the 3D migration (Fig. 4). Only the most eastern 3D migration profile shows evidence of a low velocity zone beneath the 410 in the south. Conversely, the 660 discontinuity and its associated low velocity zone are spatially consistent between both the 2D and 3D migrations. The comparison between the two sets of migrated images allows us to identify the more robust features of our data set (e.g. the location of the 660 discontinuity), alongside those features that show spatial variability that is unclear in the 1D migration, such as the low velocity zone associated with the 410.

We find strong correlation between the structure of the MTZ discontinuities and tomographic images that map broad-scale velocity variations associated with the subducted slab. The 410 and 660 both appear slightly deeper than average in the 3D migrations. With our current dataset, it is difficult to determine whether the depression of the 410 and 660 can be attributed solely to a reduction in S-wave velocity above the 410, a true depression of both discontinuities, or a combination of these two. There is little evidence for significant topography of the 410 that exceeds more than a few kilometres. This is in agreement with the tomographic models of the region, which indicates that the slab impinges on the 410 to the south of our study area (Berk Biryol et al., 2011; Piromallo and Morelli, 2003; Zhu et al., 2015). Therefore, it appears that the deepening of the 660 due to the presence of the subducted slab is the most likely cause of the increase in MTZ thickness to 270 km. Experimental values for the Clapeyron slope for the transition from ringwoodite to bridgmanite and magnesiowüstite vary from -1.0 MPa/K (Fei, 2004; Katsura, 2003) to -3.0 MPa/K (Ito and Takahashi, 1989). If we attribute the observed thickening of the MTZ purely to the ringwoodite phase transition, this would indicate a temperature reduction in the range of 1000 K to 330 K. Temperatures at the higher end of this

range seem unrealistic (Peacock, 1996; Stern, 2002). However, recent studies suggest that a disassociation of ringwoodite into akimotoite and periclase might alter the Clapeyron slope of the 660 to values of -4 to -6 MPa/K (Hernández et al., 2015; Yu et al., 2011). This would reduce the required temperature difference between the (most likely cold) slab and ambient mantle at a depth of 660 km to explain the deepening of the 660 to a more realistic ~160 to 245 K (e.g. Cottaar & Deuss, 2016).

P-to-S conversions from a depth of 520 km are observed in the centre of the profile and seem to be co-located with the top of the subducted slab. The high amplitude of this conversion would imply a strong and sharp discontinuity. The wadsleyite to ringwoodite phase transition is thought to take place over a wide depth range of 25 to 60 km (Akaogi et al., 1989) which would not be detectable in the frequency range of our data. The depth interval for the wadsleyite to ringwoodite transition has been found to be dependent on temperature (Xu et al., 2008), iron and water content (Mrosko et al., 2015). The co-location of the subducted slab and the arrivals from about 520 km depth (Fig. 3 and 4) makes it difficult to differentiate the source of these P-to-S conversions from a discontinuity formed due to a solid-solid phase transition or a compositional effect due to the top of the slab or the subducted oceanic Moho (Sinogeikin et al., 2003). The detection of an interface at this depth supports the existence of the slab in the transition zone in both scenarios, either by sharpening the phase transition through a temperature or water related effect; or by representing a direct detection of a compositional interface such as the top of the slab or the subducted Moho. The detection of a slab related interface (paleo-surface, paleo-Moho) seems to be a more suitable explanation.

Negative P-S converted energy that surrounds the 410 and occurs above the 660 is a prominent feature of this dataset and most likely indicates the presence of low velocity zones. Several studies have detected a low velocity zone above the 410 (*Revenaugh and Meyer*, 1997; *Song et al*., 2004; *Tauzin et al*., 2010) which has been interpreted as partial melting due to dehydration of hydrated material convecting upwards through the 410 (Bercovici and Karato, 2003). We observe a similar low velocity zone throughout our study region, although there is significant depth variation, most prominently a deepening from south to north. An intriguing feature of our PRFs is a negative arrival below the 410, which is interpreted as a low velocity zone at the top of the MTZ. Hydrated wadsleyite has been found to be more buoyant than dry wadsleyite (Karato, 2006), meaning hydrated material could rise to the top of

the MTZ. Hydrated wadsleyite "underplating" the 410, as suggested by *Schmerr and Garnero* [2007] beneath South America, is a candidate for the origin of this low velocity zone. The 410 is observed throughout the profile even in the presence of this deeper negative arrival so the low velocity hydrated wadsleyite does not obscure the conversion from the 410 in this location (Schmerr and Garnero, 2007). The hydration of transition zone wadsleyite may occur when the slab enters the transition zone and contains hydrous mineral phases and sediments (Kuritani et al., 2011). The detection of the low velocity layer beneath the 410 along the whole profile could be a remnant of this hydration process as the rollback of the Hellenic arc (currently 25-30 mm/yr towards the south west) (McClusky et al., 2000) would have placed the slab further to the north-east in the past, perhaps within our study region. Additionally, the 410 has a lower amplitude in the centre of the profile (Fig. 3, 4), in an area that coincides with a low velocity zone in the tomographic model (Zhu et al., 2015). This low velocity zone, along with the decreased amplitude of the 410 transition could also indicate an increased level of hydration in this area (Helffrich and Wood, 1996). However, Frost & Dolejš (2007) suggest that this effect can only occur where temperatures are significantly below ambient mantle and where water contents are at or approaching saturation. The subducted slab and the long subduction history in the region might be able to provide these necessary conditions.

The PRFs migrations also show a negative conversion above the 660. Dehydration melting, due to the larger water capacity of transition zone minerals compared to the lower mantle (Hirschmann, 2006; Pearson et al., 2014; Schmandt et al., 2014), would create a low velocity zone below the 660 in regions of down-welling. In contrast, we observe low velocities above the 660. Although the phase transition in the olivine system (from ringwoodite to bridgmanite and magnesiowüstite) can explain the large scale structure of the 660, other phase transitions from garnet to calcium-rich bridgmanite have been detected in a similar pressure and temperature range (Vacher et al., 1998). This could lead to a more complicated structure of the 660. Such complexity has been inferred from seismic observations in other subduction zones around the planet (Simmons and Gurrola, 2000; Thomas and Billen, 2009). In contrast to these studies, our observations of the 660 beneath Anatolia do not show any potential splitting in the P-to-S conversions, but instead a negative velocity layer, which cannot be explained by the proposed phase transitions. *Shen et al*. [2008] and *Shen and Blum* [2003] attribute a low velocity zone at these depths to the

sedimentation of former subducted oceanic crust onto the 660, forming a layer dominated by majorite garnet. Similar proposals have been made for structures beneath western North America by *Tauzin et al*. [2013]. This mechanism requires that the crustal part of the slab is stripped from the mantle component due to differential buoyancy (Karato, 1997), and could explain the presence of a low velocity anomaly above the 660. However, seismic evidence shows that some crustal material enters the lower mantle (Bentham et al., 2017; Kaneshima, 2016; Rost et al., 2008). Here, we observe a low velocity zone over the area of the profile where the slab seems to be lying flat on the 660. It remains unclear whether the slab is potentially overlying an older layer that contains crustal material, or if the velocity structure of the harzburgitic slab can be responsible for the low velocity anomaly atop the 660.

A further explanation for low seismic velocities within the subducted slab in the lower MTZ is the presence of dense hydrous magnesium silicate phases. Low seismic velocities were observed by Brudzinski and Chen (2003) within the Tonga slab at mid to lower MTZ depths, and while this was interpreted as being associated with a metastable olivine wedge, more recent experimental work has postulated that the presence of superhydrous Phase B (ShyB) +/- Phase D could also explain the results (Rosa et al., 2015). These phases are only stable along cold slab geotherms and have been previously linked to rapid subduction of old oceanic lithosphere along the western Pacific. The material being subducted in the Cyprus trench is believed to be comprised of ~95Ma back-arc material formed during slab roll-back in the Late Cretaceous (Maffione et al., 2017; van der Meer et al., 2018). In addition to this, the age of eastern Mediterranean oceanic crust has been suggested to be as old as 340Ma, potentially making it a remnant of the Neotethys Ocean (Granot, 2016). These ages would likely be sufficient to produce the thick and cold oceanic lithosphere required to stabilise ShyB within the subducted slab at MTZ depths (e.g. Litasov & Ohtani, 2010), making this a viable hypothesis for the observed low velocity layer within the Cyprus Slab.

Summary and Conclusions

This work studied a region of the upper mantle beneath north-western Anatolia, where the Cyprus slab passes through the MTZ. The dense imaging of the transition zone with P-to-S conversions from receiver functions allows accurate observations of the interaction between the MTZ and the subducted slab. The ‘410’ and ‘660’ are found

to be slightly deeper than the global average, though this is potentially due to low velocities in the upper mantle (Fichtner et al., 2013a; Zhu et al., 2015). The cold thermal anomaly of the subducted slab appears to deepen the 660, resulting in a mantle transition zone thickness of approximately 270 km. We estimate that this depression of the 660 translates to a negative temperature anomaly of 160 to 240 K at 660 km depth compared to ambient mantle. The 410 shows little topography and we thus conclude that the slab likely passes through the 410 to the south of our study area. The 410 is bounded by strong negative arrivals above and below the main conversion. A low velocity zone above the 410 might be related to melting of hydrated wadsleyite flowing from the transition zone and transitioning to dry olivine (Bercovici and Karato, 2003), while the low velocity zone below the 410 can be explained by buoyant hydrous wadsleyite rising to the top of the transition zone (Karato, 2006; Schmerr and Garnero, 2007). A conversion observed at a depth of ~520 km could be due to either a sharpening of the wadsleyite to ringwoodite phase transition due to the presence of the cold slab (Xu et al., 2008), the presence of water extracted from the slab (Kuritani et al., 2011), or simply a compositional signature from the subducted Moho or the top of the crust. A low velocity zone directly above the 660 might be related to mid-ocean ridge basalt that has been removed from the top of subducted slabs in the transition zone (Thomas and Billen, 2009), or could indicate the presence of dense hydrous phases within the subducted slab (e.g. ShyB +/- Phase D). The dense nature of this P-receiver function study allows the detection and characterization of a wide variety of features in the MTZ beneath Anatolia. The results suggest a complex suite of processes, involving both thermal and chemical variations, occurs within and around the MTZ during the transit of a subducted slab into the lower mantle.

Acknowledgements

This work has been supported by the UK Natural Environment Research Council under grant NE/I028017/1. Seismic equipment was provided by the NERC Geophysical Equipment Facility (SEIS-UK) under loan 947. Additional funds were provided by the Bogazici University Scientific Research Projects (BAP) under grant 6922 and the Turkish State Planning Organization (DTP) under the TAM project number 2007K120610. G.T. was supported by the Leeds-York Doctoral Training

Partnership (SPHERES) of the Natural Environment Research Council (NERC), UK (NE/L002574/1).

References

Akaogi, M., Ito, E., Navrotsky, A., 1989. Olivine-modified spinel-spinel transitions in the system Mg2SiO4 -Fe2SiO4 : Calorimetric measurements, thermochemical calculation, and geophysical application. J. Geophys. Res. Solid Earth 94, 15671–15685. https://doi.org/10.1029/JB094iB11p15671

Ammon, C.J., 1991. The isolation of receiver effects from teleseismic P-waveforms. Bull. Seismol. Soc. Am. 81, 2504–2519.

Bentham, H.L.M., Rost, S., Thorne, M.S., 2017. Fine-scale structure of the mid-mantle characterised by global stacks of PP precursors. Earth Planet. Sci. Lett. 472. https://doi.org/10.1016/j.epsl.2017.05.027

Bercovici, D., Karato, S., 2003. Whole-mantle convection and the transition-zone water filter. Nature 425, 39–44. https://doi.org/10.1038/nature01918

Berk Biryol, C., Beck, S.L., Zandt, G., Özacar, A.A., 2011. Segmented African lithosphere beneath the Anatolian region inferred from teleseismic P-wave tomography. Geophys. J. Int. 184, 1037–1057. https://doi.org/10.1111/j.1365-246X.2010.04910.x

Bijwaard, H., Spakman, W., Engdahl, E.R., 1998. Closing the gap between regional and global travel time tomography. J. Geophys. Res. Solid Earth 103, 30055–30078. https://doi.org/10.1029/98JB02467

Bock, G., 1994. Synthetic seismogram images of upper mantle structure: No evidence for a 520-km discontinuity. J. Geophys. Res. 99, 15843–15851. https://doi.org/10.1029/94JB00992

Bolfan-Casanova, N., McCammon, C.A., Mackwell, S.J., 2006. Water in transition zone and lower mantle minerals, in: Jacobsen, S.D., van der Lee, S. (Eds.), Earth's Deep Water Cycle. American Geophysical Union, pp. 57–68. https://doi.org/10.1029/168GM06

Brudzinski, M.R., Chen, W.-P., 2003. A petrologic anomaly accompanying outboard earthquakes beneath Fiji-Tonga: Corresponding evidence from broadband P and S waveforms. J. Geophys. Res. Solid Earth 108. https://doi.org/10.1029/2002JB002012

Cavazza, W., Roure, F., Spakman, W., Stampfli, G.M., Ziegler, P.A., 2004. The Transmed Atlas. The Mediterranean Region from Crust to Mantle, Springer, Berlin Heidelberg. Springer, Berlin Heidelberg. https://doi.org/10.1007/978-3-642-18919-7

Cornwell, D.G., Hetényi, G., Blanchard, T.D., 2011. Mantle transition zone variations beneath the Ethiopian Rift and Afar: Chemical heterogeneity within a hot mantle? Geophys. Res. Lett. 38, 1–6. https://doi.org/10.1029/2011GL047575

Cottaar, S., Deuss, A., 2016. Large-scale mantle discontinuity topography beneath Europe: Signature of akimotoite in subducting slabs. J. Geophys. Res. Solid Earth 121, 279–292. https://doi.org/10.1002/2015JB012452

DANA, 2012. Dense Array for North Anatolia (DANA). International Federation of Digital Seismograph Networks. https://doi.org/10.7914/SN/YH_2012

Dasgupta, R., Hirschmann, M.M., 2010. The deep carbon cycle and melting in Earth's interior. Earth Planet. Sci. Lett. 298, 1–13.

https://doi.org/10.1016/j.epsl.2010.06.039
Faccenna, C., Bellier, O., Martinod, J., 2006. Slab detachment beneath eastern Anatolia: a possible cause for the formation of the North Anatolian Fault Earth and Planetary. Sci. Lett. 242, 1–2. https://doi.org/10.1029/2002JB001757.
Farr, T.G., Rosen, P.A., Caro, E., Crippen, R., Duren, R., Hensley, S., Kobrick, M., Paller, M., Rodriguez, E., Roth, L., Seal, D., Shaffer, S., Shimada, J., Umland, J., Werner, M., Oskin, M., Burbank, D., Alsdorf, D., 2007. The Shuttle Radar Topography Mission. Rev. Geophys. 45, RG2004. https://doi.org/10.1029/2005RG000183
Fei, Y., 2004. Experimentally determined postspinel transformation boundary in Mg2SiO4 using MgO as an internal pressure standard and its geophysical implications. J. Geophys. Res. 109, 1–8. https://doi.org/10.1029/2003JB002562
Fichtner, A., Saygin, E., Taymaz, T., Cupillard, P., Capdeville, Y., Trampert, J., 2013a. The deep structure of the North Anatolian Fault Zone. Earth Planet. Sci. Lett. 1–9. https://doi.org/10.1016/j.epsl.2013.04.027
Fichtner, A., Trampert, J., Cupillard, P., Saygin, E., Taymaz, T., Capdeville, Y., Villasenor, A., 2013b. Multiscale full waveform inversion. Geophys. J. Int. 194, 534–556. https://doi.org/10.1093/gji/ggt118
Flanagan, M.P., Shearer, P.M., 1998. Global mapping of topography on transition zone velocity discontinuities by stacking SS precursors. J. Geophys. Res. Solid Earth 103, 2673–2692. https://doi.org/10.1029/97JB03212
Frost, D.J., 2008. The upper mantle and transition zone. Elements 4, 171–176. https://doi.org/10.2113/GSELEMENTS.4.3.171
Frost, D.J., Dolejš, D., 2007. Experimental determination of the effect of H2O on the 410-km seismic discontinuity. Earth Planet. Sci. Lett. 256, 182–195. https://doi.org/10.1016/J.EPSL.2007.01.023
Gilbert, H.J., Sheehan, A.F., Wiens, D.A., Dueker, K.G., Dorman, L.M., Hildebrand, J., Webb, S., 2001. Upper mantle discontinuity structure in the region of the Tonga Subduction Zone. Geophys. Res. Lett. 28, 1855–1858. https://doi.org/10.1029/2000GL012192
Goes, S., Spakman, W., Bijwaard, H., 1999. A Lower Mantle Source for Central European Volcanism. Science 286, 1928–1931.
Granot, R., 2016. Palaeozoic-aged oceanic crust preserved beneath the eastern Mediterranean. Nat. Geosci. 9, 701–705. https://doi.org/10.1038/ngeo2784
Gu, Y., Dziewonski, A.M., Agee, C.B., 1998. Global de-correlation of the topography of transition zone discontinuities. Earth Planet. Sci. Lett. 157, 57–67. https://doi.org/10.1016/S0012-821X(98)00027-2
Gu, Y.J., Dziewonski, A.M., 2002. Global variability of transition zone thickness. J. Geophys. Res. Solid Earth 107, ESE 2-1-ESE 2-17. https://doi.org/10.1029/2001JB000489
Hafkenscheid, E., Wortel, M.J.R., Spakman, W., 2006. Subduction history of the Tethyan region derived from seismic tomography and tectonic reconstructions. J. Geophys. Res. 111, 1–26. https://doi.org/10.1029/2005JB003791
Helffrich, G., 2000. Topography of the transition zone seismic discontinuities. Rev. Geophys. 38, 141. https://doi.org/10.1029/1999RG000060
Helffrich, G.R., Wood, B.J., 1996. 410 km discontinuity sharpness and the form of

the olivine α-β phase diagram: resolution of apparent seismic contradictions. Geophys. J. Int. 126, F7–F12. https://doi.org/10.1111/j.1365-246X.1996.tb05292.x
Hernández, E.R., Brodholt, J., Alfè, D., 2015. Structural, vibrational and thermodynamic properties of Mg2SiO4 and MgSiO3 minerals from first-principles simulations. Phys. Earth Planet. Inter. 240, 1–24. https://doi.org/10.1016/J.PEPI.2014.10.007
Hetényi, G., Stuart, G.W., Houseman, G. a., Horváth, F., Hegedűs, E., Brückl, E., 2009. Anomalously deep mantle transition zone below Central Europe: Evidence of lithospheric instability. Geophys. Res. Lett. 36, 1–6. https://doi.org/10.1029/2009GL040171
Hirschmann, M., 2006. Water, melting, and the deep Earth H2O cycle. Annu. Rev. Earth Planet. Sci. 34, 629–653. https://doi.org/10.1146/annurev.earth.34.031405.125211
Inoue, T., Weidner, D.J., Northrup, P.A., Parise, J.B., 1998. Elastic properties of hydrous ringwoodite (γ-phase) in Mg2SiO4. Earth Planet. Sci. Lett. 160, 107–113. https://doi.org/10.1016/S0012-821X(98)00077-6
Ito, E., Takahashi, E., 1989. Postspinel transformations in the system Mg_2SiO_4-Fe_2SiO_4 and some geophysical implications. J. Geophys. Res. Solid Earth 94, 10637–10646. https://doi.org/10.1029/JB094iB08p10637
Jolivet, L., Faccenna, C., Huet, B., Labrousse, L., Le Pourhiet, L., Lacombe, O., Lecomte, E., Burov, E., Denèle, Y., Brun, J.-P., Philippon, M., Paul, A., Salaün, G., Karabulut, H., Piromallo, C., Monié, P., Gueydan, F., Okay, A.I., Oberhänsli, R., Pourteau, A., Augier, R., Gadenne, L., Driussi, O., 2013. Aegean tectonics: Strain localisation, slab tearing and trench retreat. Tectonophysics 597–598, 1–33. https://doi.org/10.1016/j.tecto.2012.06.011
Jolivet, L., Faccenna, C., Piromallo, C., 2009. From mantle to crust: Stretching the Mediterranean. Earth Planet. Sci. Lett. 285, 198–209. https://doi.org/10.1016/j.epsl.2009.06.017
Kaneshima, S., 2016. Seismic scatterers in the mid-lower mantle. Phys. Earth Planet. Inter. 257, 105–114. https://doi.org/10.1016/j.pepi.2016.05.004
Karato, S., 2006. Remote Sensing of Hydrogen in Earth's Mantle. Rev. Mineral. Geochemistry 62, 343–375. https://doi.org/DOI: 10.2138/rmg.2006.62.15
Karato, S., 1997. On the separation of crustal component from subducted oceanic lithosphere near the 660 km discontinuity. Phys. Earth Planet. Inter. 99, 103–111. https://doi.org/10.1016/S0031-9201(96)03198-6
Katsura, T., 2003. Post-spinel transition in Mg2SiO4 determined by high P–T in situ X-ray diffractometry. Phys. Earth Planet. Inter. 136, 11–24. https://doi.org/10.1016/S0031-9201(03)00019-0
Kennett, B., Engdahl, E., Buland, R., 1995. Constraints on seismic velocities in the Earth from travel-times. Geophys. J. Int. 122, 108–124.
Kuritani, T., Ohtani, E., Kimura, J.-I., 2011. Intensive hydration of the mantle transition zone beneath China caused by ancient slab stagnation. Nat. Geosci. 4, 713–716. https://doi.org/10.1038/ngeo1250
Langston, C.A., 1979. Structure under Mount Rainier, Washington, inferred from teleseismic body waves. J. Geophys. Res. 84, 4749. https://doi.org/10.1029/JB084iB09p04749
Ligorría, J.P., Ammon, C.J., 1999. Iterative deconvolution and receiver function estimation. Bull. Seismol. Soc. Am. 89, 1395–1400.

Litasov, K., Ohtani, E., 2010. The solidus of carbonated eclogite in the system CaO–Al2O3–MgO–SiO2–Na2O–CO2 to 32GPa and carbonatite liquid in the deep mantle. Earth Planet. Sci. Lett. 295, 115–126. https://doi.org/10.1016/j.epsl.2010.03.030

Maffione, M., van Hinsbergen, D.J.J., de Gelder, G.I.N.O., van der Goes, F.C., Morris, A., 2017. Kinematics of Late Cretaceous subduction initiation in the Neo-Tethys Ocean reconstructed from ophiolites of Turkey, Cyprus, and Syria. J. Geophys. Res. Solid Earth 122, 3953–3976. https://doi.org/10.1002/2016JB013821

McClusky, S., Balassanian, S., Barka, A., Demir, C., Ergintav, S., Georgiev, I., Gurkan, O., Hamburger, M., Hurst, K., Kahle, H., Kastens, K., Kekelidze, G., King, R., Kotzev, V., Lenk, O., Mahmoud, S., Mishin, A., Nadariya, M., Ouzounis, A., Paradissis, D., Peter, Y., Prilepin, M., Reilinger, R., Sanli, I., Seeger, H., Tealeb, A., Toksöz, M.N., Veis, G., 2000. Global Positioning System constraints on plate kinematics and dynamics in the eastern Mediterranean and Caucasus. J. Geophys. Res. Solid Earth 105, 5695–5719. https://doi.org/10.1029/1999JB900351

Mrosko, M., Koch-Müller, M., McCammon, C., Rhede, D., Smyth, J.R., Wirth, R., 2015. Water, iron, redox environment: effects on the wadsleyite–ringwoodite phase transition. Contrib. to Mineral. Petrol. 170, 9. https://doi.org/10.1007/s00410-015-1163-2

Ohtani, E., 2005. Water in the Mantle. Elements 1.

Paul, A., Karabulut, H., Mutlu, A.K., Salaün, G., 2014. A comprehensive and densely sampled map of shear-wave azimuthal anisotropy in the Aegean-Anatolia region. Earth Planet. Sci. Lett. 389, 14–22. https://doi.org/10.1016/j.epsl.2013.12.019

Peacock, S.M., 1996. Thermal and Petrologic Structure of Subduction Zones, in: Bebout, G.E., Scholl, D.W., Kirby, S.H., Platt, J.P. (Eds.), Subduction Top to Bottom. American Geophysical Union, Washington, D.C., pp. 119–133. https://doi.org/10.1029/GM096p0119

Pearson, D.G., Brenker, F.E., Nestola, F., McNeill, J., Nasdala, L., Hutchison, M.T., Matveev, S., Mather, K., Silversmit, G., Schmitz, S., Vekemans, B., Vincze, L., 2014. Hydrous mantle transition zone indicated by ringwoodite included within diamond. Nature 507, 221–224. https://doi.org/10.1038/nature13080

Pichon, X. Le, Angelier, J., 1979. The hellenic arc and trench system: A key to the neotectonic evolution of the eastern mediterranean area. Tectonophysics 60, 1–42. https://doi.org/10.1016/0040-1951(79)90131-8

Pichon, X.L., Angelier, J., Osmaston, M.F., Stegena, L., 1981. The Aegean Sea [and Discussion]. Philos. Trans. R. Soc. A Math. Phys. Eng. Sci. 300, 357–372. https://doi.org/10.1098/rsta.1981.0069

Piromallo, C., Morelli, A., 2003. P wave tomography of the mantle under the Alpine-Mediterranean area. J. Geophys. Res. Earth 108. https://doi.org/10.1029/2002JB001757

Revenaugh, J., Meyer, R., 1997. Seismic evidence of partial melt within a possibly ubiquitous low-velocity layer at the base of the mantle. Science (80-.). 277, 670–673.

Revenaugh, J., Sipkin, S., 1994. Seismic evidence for silicate melt atop the 410-km mantle discontinuity. Nature 369, 474–476.

Robertson, A.H.F., Dixon, J.E., 1984. Introduction: aspects of the geological evolution of the Eastern Mediterranean. Geol. Soc. London, Spec. Publ. 17, 1–74. https://doi.org/10.1144/GSL.SP.1984.017.01.02
Rosa, A.D., Sanchez-Valle, C., Wang, J., Saikia, A., 2015. Elasticity of superhydrous phase B, seismic anomalies in cold slabs and implications for deep water transport. Phys. Earth Planet. Inter. 243, 30–43. https://doi.org/10.1016/J.PEPI.2015.03.009
Rost, S., Garnero, E., Williams, Q., 2008. Seismic array detection of subducted oceanic crust in the lower mantle. J. Geophys. Res. 113.
Saikia, A., Frost, D.J., Rubie, D.C., 2008. Splitting of the 520-kilometer seismic discontinuity and chemical heterogeneity in the mantle. Science 319, 1515–8. https://doi.org/10.1126/science.1152818
Salaün, G., Pedersen, H.A., Paul, A., Farra, V., Karabulut, H., Hatzfeld, D., Papazachos, C., Childs, D.M., Pequegnat, C., 2012. High-resolution surface wave tomography beneath the Aegean-Anatolia region: constraints on upper-mantle structure. Geophys. J. Int. 190, 406–420. https://doi.org/10.1111/j.1365-246X.2012.05483.x
Schmandt, B., Jacobsen, S.D., Becker, T.W., Liu, Z., Dueker, K.G., 2014. Dehydration melting at the top of the lower mantle. Science (80-.). 344, 1265–1268. https://doi.org/10.1126/science.1253358
Schmerr, N., Garnero, E., 2006. Investigation of upper mantle discontinuity structure beneath the central Pacific using SS precursors. J. Geophys. Res. 111.
Schmerr, N., Garnero, E.J., 2007. Upper Mantle Discontinuity Topography from Thermal and Chemical Heterogeneity. Science (80-.). 318, 623–626. https://doi.org/10.1126/science.1145962
Shearer, P., Masters, T., 1992. Global mapping of topography on the 660-km discontinuity. Nature 355, 791–796.
Shearer, P.M., 1990. Seismic imaging of the upper mantle structure with new evidence for a 520-km discontinuity. Nature 344, 121–126. https://doi.org/10.1038/346183a0
Sheehan, A.F., Shearer, P.M., Gilbert, H.J., Dueker, K.G., 2000. Seismic migration processing of *P-SV* converted phases for mantle discontinuity structure beneath the Snake River Plain, western United States. J. Geophys. Res. Solid Earth 105, 19055–19065. https://doi.org/10.1029/2000JB900112
Shen, X., Zhou, H., Kawakatsu, H., 2008. Mapping the upper mantle discontinuities beneath China with teleseismic receiver functions. Earth, Planets Sp. 60, 713–719. https://doi.org/10.1186/BF03352819
Shen, Y., Blum, J., 2003. Seismic evidence for accumulated oceanic crust above the 660-km discontinuity beneath southern Africa. Geophys. Res. Lett. 30. https://doi.org/10.1029/2003GL017991
Simmons, N.A., Gurrola, H., 2000. Multiple seismic discontinuities near the base of the transition zone in the Earth ' s mantle. Nat. Lett. 405, 559–562. https://doi.org/10.1038/35014589
Sinogeikin, S., 2003. Single-crystal elasticity of ringwoodite to high pressures and high temperatures: implications for 520 km seismic discontinuity. Phys. Earth Planet. Inter. 136, 41–66. https://doi.org/10.1016/S0031-9201(03)00022-0
Sinogeikin, S. V, Bass, J.D., Katsura, T., 2003. Single-crystal elasticity of

ringwoodite to high pressures and high temperatures: implications for 520 km seismic discontinuity. Phys. Earth Planet. Inter. 136, 41–66. https://doi.org/10.1016/S0031-9201(03)00022-0
Smyth, J.R., Frost, D.J., 2002. The effect of water on the 410-km discontinuity: An experimental study. Geophys. Res. Lett. 29, 1–4. https://doi.org/10.1029/2001GL014418
Song, T., Helmberger, D., Grand, S., 2004. Low-velocity zone atop the 410-km seismic discontinuity in the northwestern United States. Nature 427, 530–533. https://doi.org/10.1038/nature02231
Stampfli, G.M., 2000. Tethyan oceans. Geol. Soc. London, Spec. Publ. 173, 1–23. https://doi.org/10.1144/GSL.SP.2000.173.01.01
Stern, R.J., 2002. Subduction zones. Rev. Geophys. 40. https://doi.org/10.1029/2001RG000108
Stoffa, P.L., Buhl, P., Diebold, J.B., Wenzel, F., 1981. Direct mapping of seismic data to the domain of intercept time and ray parameter—A plane-wave decomposition. GEOPHYSICS 46, 255–267. https://doi.org/10.1190/1.1441197
Tauzin, B., Debayle, E., Wittlinger, G., 2010. Seismic evidence for a global low-velocity layer within the Earth's upper mantle. Nat. Geosci. 3, 718–721. https://doi.org/10.1038/ngeo969
Tauzin, B., van der Hilst, R.D., Wittlinger, G., Ricard, Y., 2013. Multiple transition zone seismic discontinuities and low velocity layers below western United States. J. Geophys. Res. Solid Earth 118, 2307–2322. https://doi.org/10.1002/jgrb.50182
Thomas, C., Billen, M., 2009. Upper mantle structure along a profile in the Southwest Pacific. Geophys. J. Int. 176, 113–125.
Thompson, D.A., Helffrich, G., Bastow, I.D., Kendall, J.-M., Wookey, J., Eaton, D.W., Snyder, D.B., 2011. Implications of a simple mantle transition zone beneath cratonic North America. Earth Planet. Sci. Lett. 312, 28–36. https://doi.org/10.1016/j.epsl.2011.09.037
Vacher, P., Mocquet, A., Sotin, C., 1998. Computation of seismic profiles from mineral physics: the importance of the non-olivine components for explaining the 660 km depth discontinuity. Phys. Earth Planet. Inter. 106, 275–298. https://doi.org/10.1016/S0031-9201(98)00076-4
van der Meer, D.G., Spakman, W., van Hinsbergen, D.J.J., Amaru, M.L., Torsvik, T.H., 2009. Towards absolute plate motions constrained by lower-mantle slab remnants. Nat. Geosci. 3, 36–40. https://doi.org/10.1038/ngeo708
van der Meer, D.G., van Hinsbergen, D.J.J., Spakman, W., 2018. Atlas of the underworld: Slab remnants in the mantle, their sinking history, and a new outlook on lower mantle viscosity. Tectonophysics 723, 309–448. https://doi.org/10.1016/J.TECTO.2017.10.004
Van der Voo, R., Spakman, W., Bijwaard, H., 1999. Tethyan subducted slabs under India. Earth Planet. Sci. Lett. 171, 7–20. https://doi.org/10.1016/S0012-821X(99)00131-4
Xu, W., Lithgowbertelloni, C., Stixrude, L., Ritsema, J., 2008. The effect of bulk composition and temperature on mantle seismic structure. Earth Planet. Sci. Lett. 275, 70–79. https://doi.org/10.1016/j.epsl.2008.08.012
Yu, Y.G., Wentzcovitch, R.M., Vinograd, V.L., Angel, R.J., 2011. Thermodynamic properties of MgSiO3 majorite and phase transitions near 660 km depth in

MgSiO3 and Mg2SiO4 : A first principles study. J. Geophys. Res. 116, B02208. https://doi.org/10.1029/2010JB007912
Zhu, H., Bozdăg, E., Tromp, J., 2015. Seismic structure of the European upper mantle based on adjoint tomography. Geophys. J. Int. 201, 18–52. https://doi.org/10.1093/gji/ggu492

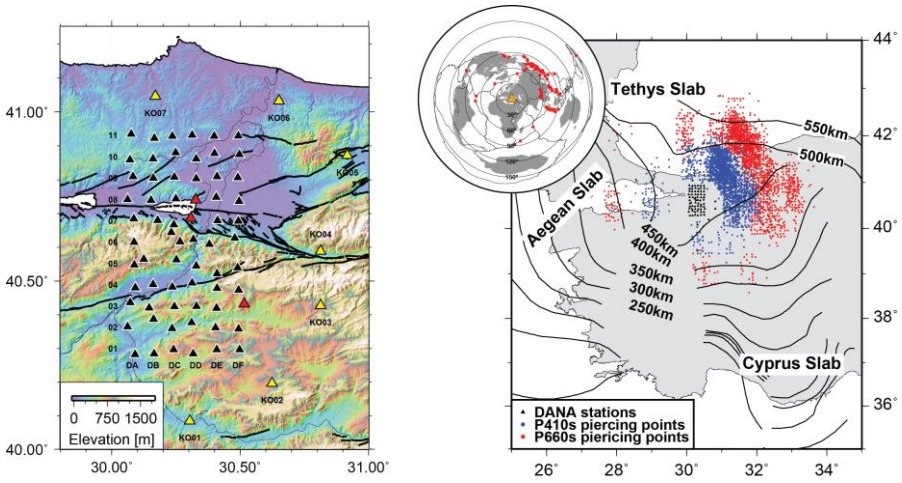

Figure 1: a) DANA station locations. Stations of the regular grid are shown as black triangles and include 3 permanent stations of the KOERI national seismic network (red triangles). Yellow triangles indicate the eastern girdle of stations with larger station spacing. Background shows elevations from the Shuttle Radar Topography mission (Farr et al., 2007). b) Receiver function piercing points at 410 km (blue) and 660 km depth (red). Station locations indicated by small triangles. Slab depths from tomographic models are indicated by black lines and are from *Berk Biryol et al*., [2011].

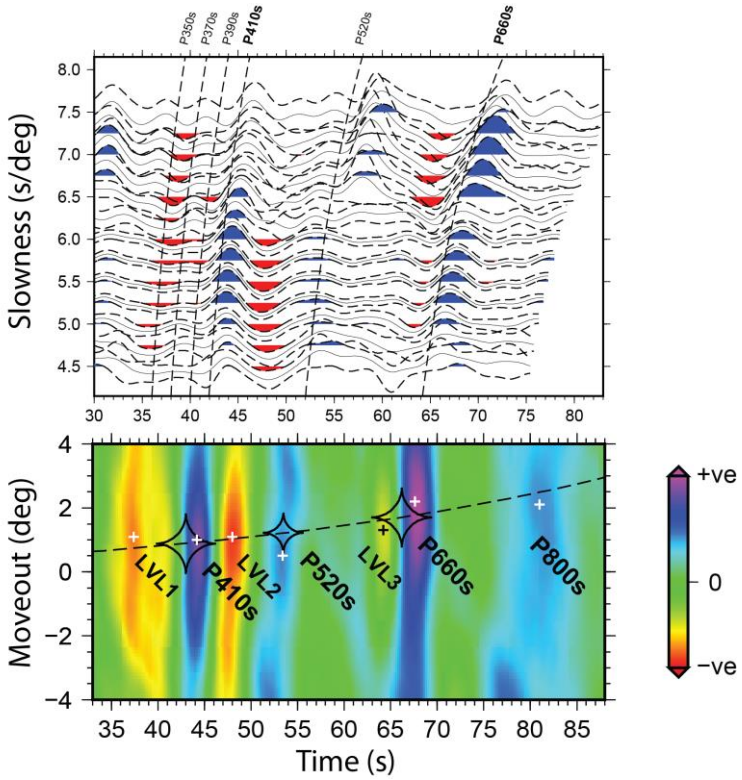

Figure 2: a) Slowness section for the DANA network using the full dataset, highlighting the arrivals from the 410-km and 660-km discontinuities and waveform variations from velocity variations. Predicted traveltimes for conversions from varying depths (dashed lines) have been calculated through the 1D Earth model ak135 (Kennett et al., 1995). Also visible are conversions from an apparent depth of 520 km in some regions of the study area. Dashed lines are 2σ confidence limits. b) Slant stack of receiver functions with a reference slowness of 5.59 s/deg. We observe strong arrivals from the 410 and 660 with strong low velocity zones around the 410 and a weaker conversion from 520 km depth. A diffuse arrival from depths of about 800 km can also be observed. The 410 arrival shows strong negative arrivals from shallower and larger depths. Similarly, a lateral varying negative arrival can be observed for the 660.

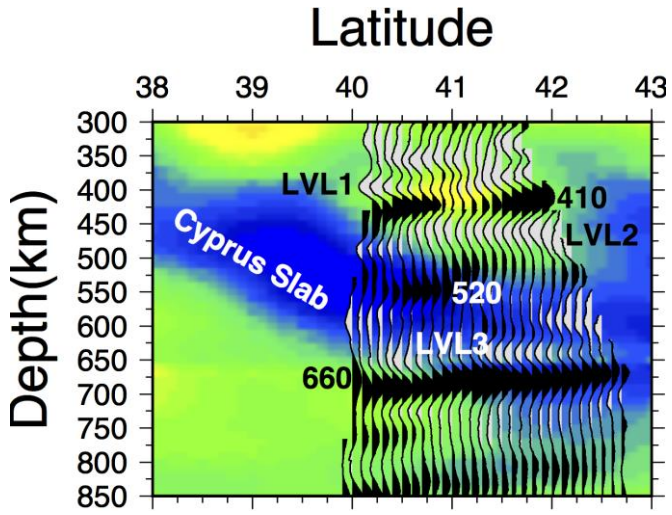

Figure 3: Common conversion point depth migrated receiver functions of the quality-controlled dataset projected onto a single NS profile using the 1D ak135 velocity model. Background shows P-wave velocity variation of tomography model EU60 (Zhu et al., 2015). The location of the slab is indicated by high seismic velocities. The positive conversions from the 410 and 660 are observable across the profile and there is evidence for a conversion from a depth of about 520 km. The PRFs show evidence for 3 low velocity layers (LVL1, LVL2, LVL3) marked by strong negative arrivals. The depth migrated section of the full dataset is shown in Suppl. Figure 1 and shows only subtle differences. Only bins containing greater than 10 traces were included in the 2D migration.

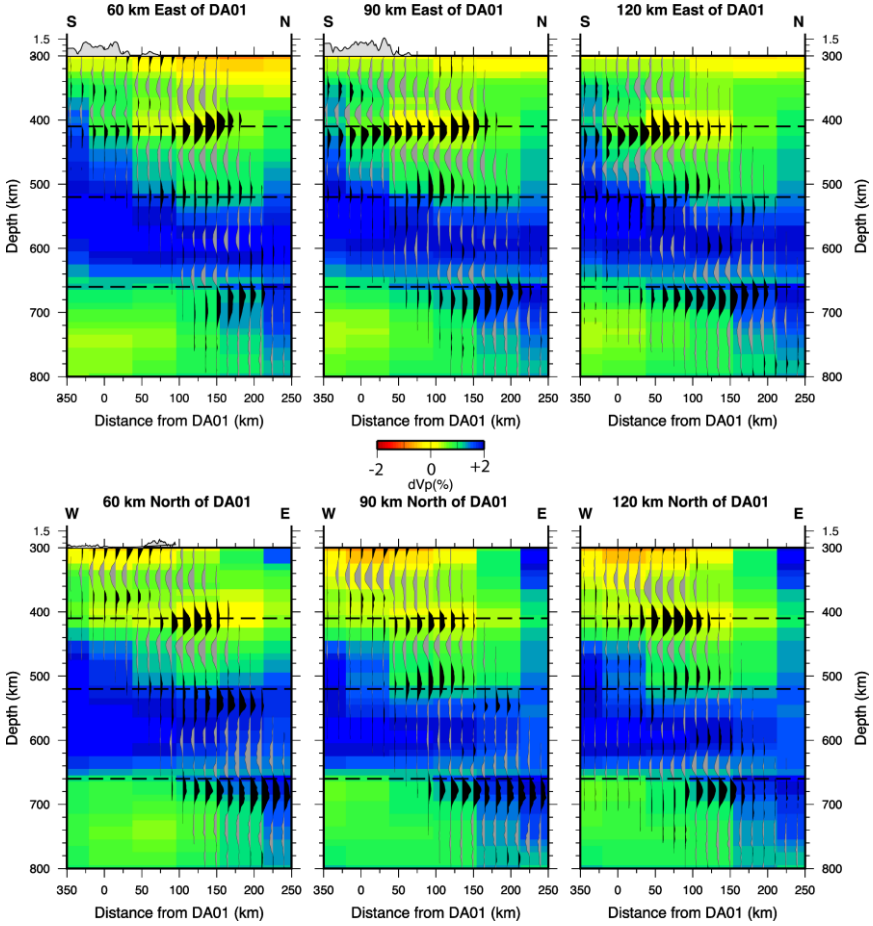

Figure 4: 3D common-conversion point (CCP) migration of the 1505 highest quality receiver functions using the EU60 regional tomography model [background colour fill, *Zhu et al*., 2015]. Color scale for tomography shown in Fig. 3. Slices through the 3D model are shown in E-W and N-S direction (at latitudes of 40.82°, 41.09° and 41.37°; and longitudes of 30.63°, 30.90°, and 31.17°). PRFs are shown as lines with positive arrivals filled in black and negative arrivals grey. Only bins containing more than 5 receiver functions are included, with a mean hit count of ~15 and maximum of 89 in the center of the study region.

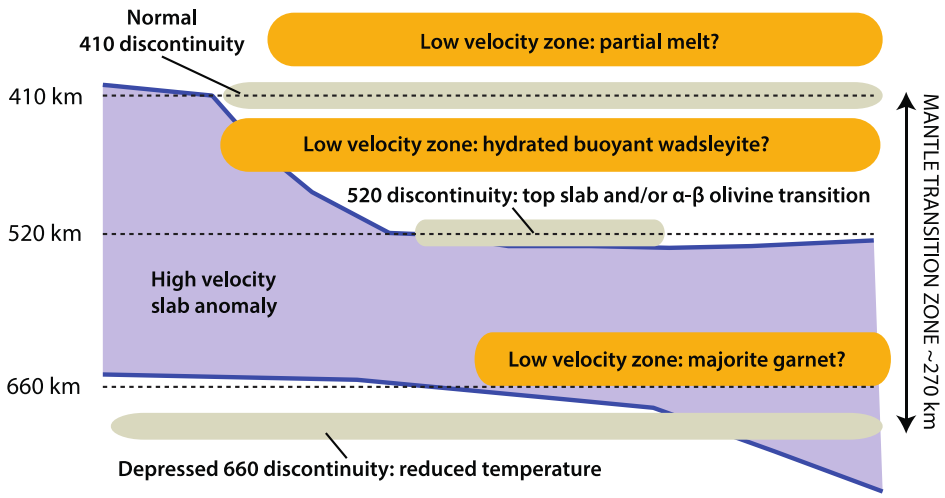

Figure 5: Interpretative sketch of the detected structure. The 410 shows little depth variation while we observe a depressed 660 due to the cooling effect of the slab. A P-S conversion from 520 km depth can be seen which could be the top of the slab or a sharpened wadsleyite to ringwoodite transition. The 410 is surrounded by low velocity zones which are related to hydration from the subducting slab. The origin of the low velocity zone above the 660 is unknown but could be related to mid-ocean ridge basalt material.